

# The formation of spiral arms and rings in barred galaxies

M. Romero-Gómez<sup>1,2</sup>, E. Athanassoula<sup>1</sup>, J.J. Masdemont<sup>3</sup>, and C. García-Gómez<sup>2</sup>

<sup>1</sup> LAM, Observatoire Astronomique de Marseille Provence, CNRS, 2 Place Le Verrier, 13248 Marseille Cédex 04, France

<sup>2</sup> D.E.I.M., Universitat Rovira i Virgili, Campus Sescelades, Avd. dels Països Catalans 26, 43007 Tarragona, Spain

<sup>3</sup> I.E.E.C & Dep. Mat. Aplicada I, Universitat Politècnica de Catalunya, Diagonal 647, 08028 Barcelona, Spain

Received 19 March

**Abstract.** In this and in a previous paper (Romero-Gómez et al. 2006) we propose a theory to explain the formation of both spirals and rings in barred galaxies using a common dynamical framework. It is based on the orbital motion driven by the unstable equilibrium points of the rotating bar potential. Thus, spirals, rings and pseudo-rings are related to the invariant manifolds associated to the periodic orbits around these equilibrium points. We examine the parameter space of three barred galaxy models and discuss the formation of the different morphological structures according to the properties of the bar model. We also study the influence of the shape of the rotation curve in the outer parts, by making families of models with rising, flat, or falling rotation curves in the outer parts. The differences between spiral and ringed structures arise from differences in the dynamical parameters of the host galaxies. The results presented here will be discussed and compared with observations in a forthcoming paper.

**Key words.** galaxies – structure – ringed galaxies – spiral arms – barred galaxies

## 1. Introduction

Bars are a very common feature of disc galaxies. In a sample of 186 spirals drawn from the Ohio State University Bright Spiral Galaxy Survey, Eskridge et al. (2000) find that in the near infrared 56% of the galaxies are strongly barred, while an additional 6% are weakly barred. Only 27% can be classified as non-barred. A large fraction of barred galaxies show two clearly defined spiral arms (e.g. Elmegreen & Elmegreen 1982), often departing from the end of the bar at nearly right angles. This is the case for instance in NGC 1300, NGC 1365 and NGC 7552. Deep exposures, moreover, show that these arms wind around the bar structure and extend to large distances from the centre (see for instance Sandage & Bedke 1994). Almost all researchers agree that spiral arms and rings are driven by the gravitational field of the galaxy (see Toomre 1977 and Athanassoula 1984, for reviews). In particular, spirals are believed to be density waves in a disc galaxy (Lindblad 1963). Toomre (1969) found that the spiral waves propagate towards the principal Lindblad resonances of the galaxy, where they damp down, and thus concludes that long-lived spirals need some replenishment.

There are essentially three different possibilities for a spiral wave to be replenished. First, it can be driven by a companion or satellite galaxy. A direct, relatively slow and close passage of another galaxy can form trailing shapes (e.g. Toomre 1969; Toomre & Toomre 1972; Goldreich & Tremaine 1978, 1979;

Toomre 1981 and references therein). They can also be excited by the presence of a bar. Several studies have shown that a rotating bar or oval can drive spirals (e.g. Lindblad 1960; Toomre 1969; Sanders & Huntley 1976; Schwarz 1979, 1981; Huntley 1980). Athanassoula (1980) studied the self-consistent quasi-stationary response of a galaxy composed of both gas and stars to a growing and rotating bar. She showed that the response of both components is bar-like up to corotation, where it turns into a trailing two-armed spiral, ending approximately at the Outer Lindblad Resonance (OLR). The third alternative, proposed by Toomre (1981), is the swing amplification feedback cycle. This starts with a leading wave propagating from the center towards corotation. In doing so, it unwinds and then winds in the trailing sense, while being very strongly amplified. This trailing wave will propagate towards the center, while a further trailing wave is emitted at CR and propagates outwards, where it is dissipated at the OLR. The inwards propagating trailing wave, when reaching the center will reflect into a leading spiral which will propagate outwards towards the CR, thus closing the feedback cycle. Note that, if there is an Inner Lindblad Resonance (ILR), the wave propagating inwards is damped at that resonance and the cycle is cut.

Strongly barred galaxies can also show prominent and spectacular rings or partial rings. The origin of such morphologies has been studied by Schwarz (1981, 1984, 1985), who followed the response of a gaseous disc galaxy to a bar perturbation. He proposed that ring-like patterns are associated to the principal orbital resonances, namely ILR, CR, and OLR. The ILR would be responsible for the nuclear rings, CR would

be associated with the inner rings, which are indicated by an  $r$  in the de Vaucouleurs classification, and the OLR would be the origin of the outer rings, which are indicated by an  $R$  preceding the Hubble type. Nuclear rings are small rings of star formation often found near the centres or nuclei of early-type barred galaxies, but we will not discuss these structures here. Inner rings are the well-defined rings that encircle the bars of barred galaxies. They are sometimes active sites of star formation. Outer rings are the larger, more diffuse rings, about twice the size of the bar. When these structures are incomplete, we designate them with the term pseudo-rings. There are different types of outer rings. Buta (1995) classified them according to the relative orientation of the ring and bar major axes. If these two axes are perpendicular, the shape of the ring is similar to an “8” and the outer ring is classified as  $R_1$ . If the two axes are parallel, the outer ring is classified as  $R_2$ . Finally, if both types of rings are present in the galaxy, the outer ring is classified as  $R_1R_2$ .

In this paper, we develop further the basic idea that we proposed in a previous paper (Romero-Gómez et al. 2006, hereafter Paper I). Rings and spiral arms are the result of the orbital motion driven by the invariant manifolds associated to periodic orbits around unstable equilibrium points. In Paper I we gave a complete and thorough description of the dynamical framework and, as an example, specifically calculated the orbital evolution of a particular type of  $rR_1$  ringed galaxy. In this paper, we construct families of models based on simple, yet realistic, barred galaxy potentials. In each family, we vary one of the free parameters of the potential and keep the remaining fixed. For each model, we compute numerically the orbital structure associated to the invariant manifolds. In this way, we are able to study the influence of each model parameter on the global morphologies delineated by the invariant manifolds.

In Sect. 2, we present the equations of motion and the galactic models that will be used for the computations. In Sect. 3, we give a brief description of the invariant manifolds and describe their role in the transfer of matter within the galaxy. In Sect. 4, we show the different morphologies that result from the computations of each model and in Sect. 5 we briefly summarize. Applications to real galaxies, as well as comparisons with observations and with other theoretical work (Schwarz 1981, 1984, 1985; Kaufmann & Contopoulos 1996; Patsis 2006; Voglis, Stavropoulos & Kalapotharakos 2006) will be given in paper III of this series.

## 2. Models

### 2.1. Equations of motion and equilibrium points

We model the potential of a barred galaxy as the superposition of three components, two of them axisymmetric and the third bar-like. This latter component rotates anti-clockwise with angular velocity  $\mathbf{\Omega}_p = \Omega_p \mathbf{z}$ , where  $\Omega_p$  is a constant pattern speed<sup>1</sup>. The equations of motion in this potential in a frame rotating with angular speed  $\mathbf{\Omega}_p$  in vector form are

$$\ddot{\mathbf{r}} = -\nabla\Phi - 2(\mathbf{\Omega}_p \times \dot{\mathbf{r}}) - \mathbf{\Omega}_p \times (\mathbf{\Omega}_p \times \mathbf{r}), \quad (1)$$

where the terms  $-2\mathbf{\Omega}_p \times \dot{\mathbf{r}}$  and  $-\mathbf{\Omega}_p \times (\mathbf{\Omega}_p \times \mathbf{r})$  represent the Coriolis and the centrifugal forces, respectively, and  $\mathbf{r}$  is the position vector.

Following Binney & Tremaine (1987), we take the dot product of Eq. (1) with  $\dot{\mathbf{r}}$ , and by rearranging the resulting equation, we obtain

$$\frac{dE_J}{dt} = 0,$$

where

$$E_J \equiv \frac{1}{2} |\dot{\mathbf{r}}|^2 + \Phi - \frac{1}{2} |\mathbf{\Omega}_p \times \mathbf{r}|^2.$$

The quantity  $E_J$  is a constant of the motion and is known as the Jacobi integral, or as the Jacobi constant. Note that it is the sum of  $\frac{1}{2}\dot{\mathbf{r}}^2 + \Phi$ , which is the energy in a non-rotating frame, and of the quantity

$$-\frac{1}{2} |\mathbf{\Omega}_p \times \mathbf{r}|^2 = -\frac{1}{2} \Omega_p^2 (x^2 + y^2),$$

which can be thought of as the “potential energy” to which the centrifugal “force” gives rise. Thus, if we define an effective potential

$$\Phi_{\text{eff}} = \Phi - \frac{1}{2} \Omega_p^2 (x^2 + y^2),$$

Eq. (1) becomes

$$\ddot{\mathbf{r}} = -\nabla\Phi_{\text{eff}} - 2(\mathbf{\Omega}_p \times \dot{\mathbf{r}}),$$

and the Jacobi constant is

$$E_J = \frac{1}{2} |\dot{\mathbf{r}}|^2 + \Phi_{\text{eff}},$$

which, being constant in time, can be considered as the energy in the rotating frame.

Setting  $x_1 = x$ ,  $x_2 = y$ ,  $x_3 = \dot{x}$ , and  $x_4 = \dot{y}$ , we can write the components of the equations of motion as

$$\begin{cases} \dot{x}_1 = f_1(x_1, x_2, x_3, x_4) = x_3 \\ \dot{x}_2 = f_2(x_1, x_2, x_3, x_4) = x_4 \\ \dot{x}_3 = f_3(x_1, x_2, x_3, x_4) = 2\Omega_p x_4 - \Phi_x \\ \dot{x}_4 = f_4(x_1, x_2, x_3, x_4) = -2\Omega_p x_3 - \Phi_y, \end{cases} \quad (2)$$

where we have defined  $\Phi_x = \frac{\partial\Phi_{\text{eff}}}{\partial x}$  and  $\Phi_y = \frac{\partial\Phi_{\text{eff}}}{\partial y}$ . Note that we restrict ourselves to the  $z = 0$  plane because the motion in the vertical direction essentially consists of an uncoupled harmonic oscillator and does not affect the motion in this plane (see Paper I).

The surface  $\Phi_{\text{eff}} = E_J$  is called the zero velocity surface, and its intersection with the  $z = 0$  plane gives the zero velocity curve. All regions in which  $\Phi_{\text{eff}} > E_J$  are forbidden to a star with this energy, and are thus called forbidden regions. The zero velocity curve also defines two different regions, namely, an exterior region and an interior one that contains the bar. The interior and exterior regions are connected via the equilibrium points (see Fig. 2b of Paper I).

The bar component is rotating as a solid body with a constant pattern speed  $\Omega_p$ . For our calculations we place ourselves in a frame of reference corotating with the bar, and the bar semi-major axis is located along the  $x$  axis. In this rotating frame we have five equilibrium Lagrangian points. Three of

<sup>1</sup> Bold letters denote vector notation. The vector  $\mathbf{z}$  is a unit vector.

these points are stable, namely  $L_3$ , which is placed at the centre of the system, and  $L_4$  and  $L_5$ , which are located symmetrically on the  $y$  axis. The two equilibrium points left,  $L_1$  and  $L_2$ , are unstable and are located symmetrically on the  $x$  axis. The position of the corotation radius will be determined by the free parameter  $r_L$ , that is, the distance from the centre to  $L_1$ , or, equivalently, to  $L_2$ , because the model is symmetric with respect to both  $x$  and  $y$  axes. In our case, we choose  $r_L$  to be the distance from the centre to  $L_1$ . The pattern speed is related to  $r_L$  through the expression

$$\Omega_p^2 = r_L \left( \frac{\partial \Phi(r)}{\partial r} \right)_{r_L}, \quad (3)$$

where  $\Phi(r)$  is the potential on the equatorial plane.

## 2.2. Galaxy models and free parameters

In this section we describe the potentials that we use to model a barred galaxy. Our basic model will be the one introduced by Athanassoula (1992a) in a thorough study of the orbital structure of bars. The axisymmetric component consists of the superposition of a disc and a spheroid, whose basic parameters are determined so that the rotation curve of the galactic model has the desired characteristics. The disc is modelled as a Kuzmin-Toomre disc (Kuzmin 1956; Toomre 1963) of surface density

$$\sigma(r) = \frac{V_d^2}{2\pi r_d} \left( 1 + \frac{r^2}{r_d^2} \right)^{-3/2}. \quad (4)$$

The parameters  $V_d$  and  $r_d$  set the scales of the velocities and radii, respectively. The spheroid is modelled using a density distribution of the form

$$\rho(r) = \rho_b \left( 1 + \frac{r^2}{r_b^2} \right)^{-3/2}, \quad (5)$$

where  $\rho_b$  and  $r_b$  determine its concentration and scale length. Spheroids with high concentration have high values of  $\rho_b$  and small values of  $r_b$ , the opposite being true for spheroids of low concentration. Although we give two separate axisymmetric components, it is important to note that, in fact, what matters in this study is only the total axisymmetric rotation curve and not its decomposition into components.

The bar component is described by a Ferrers (1877) ellipsoid whose density distribution is described by the expression:

$$\begin{cases} \rho_0(1 - m^2)^n & m \leq 1 \\ 0 & m \geq 1, \end{cases} \quad (6)$$

where  $m^2 = x^2/a^2 + y^2/b^2$ . The values of  $a$  and  $b$  determine the shape of the bar,  $a$  being the length of the semi-major axis, which is placed along the  $x$  coordinate axis, and  $b$  being the length of the semi-minor axis. The parameter  $n$  measures the degree of concentration of the bar. High values of  $n$  correspond to a high concentration, while a value of  $n = 0$  is the extreme case of a constant density bar. The parameter  $\rho_0$  represents the bar central density. For these models, the quadrupole moment of the bar is given by the expression

$$Q_m = M_b(a^2 - b^2)/(5 + 2n),$$

where  $M_b$  is the mass of the bar, equal to

$$M_b = 2^{(2n+3)} \pi a b^2 \rho_0 \Gamma(n+1) \Gamma(n+2) / \Gamma(2n+4)$$

and  $\Gamma$  is the gamma function. Throughout this paper we will use the following system of units: For the mass unit we take a value of  $10^6 M_\odot$ , for the length unit a value of 1 kpc and for the velocity unit a value of  $1 \text{ km s}^{-1}$ . Using these values, the unit of the Jacobi constant will be  $1 \text{ km}^2 \text{ s}^{-2}$ .

For reasons of continuity and to allow in Paper III a comparison of our results with the results of gas flow in these models (Athanassoula 1992b), we will use the same numerical values for the model parameters as in Athanassoula (1992a). We will hereafter refer to this model as model A. It has essentially four free parameters which determine the dynamics in the bar region. The axial ratio  $a/b$  and the quadrupole moment (or mass) of the bar  $Q_m$  (or  $M_b$ ), will determine the strength of the bar. The third parameter is the bar angular velocity, or pattern speed, determined by the Lagrangian radius  $r_L$  (Eq. 3). The last free parameter is the central concentration of the model  $\rho_c = \rho_b + \rho_0$ . As already mentioned, the basic values for the free parameters are set as in run 001 of Athanassoula (1992a):  $a/b = 2.5$ ,  $r_L = 6$ ,  $Q_m = 4.5 \times 10^4$ ,  $\rho_c = 2.4 \times 10^4$ . Then a range around each of these values is explored. The axisymmetric component is fixed by setting a maximum disc circular velocity of 164.204 at  $r = 20$ , and  $r_b$  is determined by fixing the total mass of the spheroid and bar components within  $r = 10$  to  $4.87333 \times 10^4$ , while fixing the combined central density of the bar and bulge to  $\rho_c$ . The length of the bar is fixed to 5. Results on the orbital structure underlying spirals and rings in such models will be presented in Sect. 4.1.

So far, we have followed exactly the model of Athanassoula (1992a). Nevertheless, in this paper we are interested in spirals and rings which occur beyond or around CR, contrary to Athanassoula (1992a, 1992b), who concentrated on orbital structure and gas flow within and around the bar region. We will, therefore, consider a further option, namely whether the rotation curve in the region beyond CR is flat (model F), or somewhat rising (model R), or somewhat falling (model D). This will be achieved by considering the same axisymmetric components as in model A, but with different values of the parameters. The different shapes of the rotation curve in the outer parts are obtained by giving different maximum disc circular velocities at a fixed radius. Thus, model R, with a rising rotation curve, has a maximum disc circular velocity of 164.204 at  $r = 20$ . Model F, with a flat rotation curve in the outer parts, has a maximum disc circular velocity of 100 at  $r = 20$ , while model D, with a decreasing rotation curve in the outer parts, has a maximum disc circular velocity of 10 at  $r = 20$ . The spheroid scale length is determined as in model A. In this case, we use an inhomogeneous Ferrers bar ( $n = 1$ ) with axial ratio  $a/b = 2.5$  and a semi-major axis  $a = 5$ , and a central concentration  $\rho_c = 0.05 \times 10^4$ . The basic values for the remaining free parameters are taken to be  $r_L = 6$  and  $Q_m = 4.5 \times 10^4$ . As for the previous model, a range around each of these values is explored. Results using these models are presented in Sect. 4.2.

The Ferrers bars are realistic models of bars and have been widely used so far in orbital structure studies within and in the immediate neighbourhood of bars (e.g. Athanassoula

et al. 1983; Pfenniger 1984, 1987, 1990; Skokos, Patsis & Athanassoula 2002a, 2002b). They contain parameters with physical meaning, such as the bar mass or axial ratio, that can be obtained from, or compared to, observations. They have, however, one disadvantage, namely that in models using such bars the ratio of the non-axisymmetric component of the force to the axisymmetric component of the force decreases very abruptly beyond a certain radius so that the axisymmetric component dominates in the outer regions. This is of no importance if one is interested in the orbital structure or the gas flow in the bar region, but in studies like this one, where one is interested in the region outside the bar, this may introduce a bias, since models with high nonaxisymmetric forces beyond CR will not be studied. In order to remedy this, we introduce two other models, also often used in the literature, which have an ad hoc bar potential, i.e. a potential that is not associated with a particular density distribution. Ad hoc models have some disadvantages. They are simple mathematical expressions for the potential and do not originate from a realistic density distribution. This means that the corresponding density distribution may have some undesired features, e.g. for very strong nonaxisymmetric perturbations the local density could even be negative. Furthermore, they do not contain simple parameters that can be directly and straightforwardly associated to observable quantities, like the bar length, mass, or axial ratio. Most of them are of the form  $\epsilon A(r) \cos(2\theta)$ , i.e. contain no  $\cos(m\theta)$  terms with  $m > 2$ . This means that the parameter  $\epsilon$  is associated with the mass of the bar and that there is no parameter to regulate its axial ratio. Despite all these shortcomings, ad hoc potentials have been widely used because they have the important advantage of being adaptable to the problem at hand, i.e. with a proper choice of the function  $A(r)$  one can obtain a potential with the desired properties, for example, in our case, a potential with an important  $m = 2$  contribution between CR and OLR.

The first ad hoc potential we use has the form

$$\Phi(r, \theta) = -\frac{1}{2}\epsilon v_0^2 \cos(2\theta) \begin{cases} 2 - \left(\frac{r}{\alpha}\right)^n, & r \leq \alpha \\ \left(\frac{\alpha}{r}\right)^n, & r \geq \alpha. \end{cases} \quad (7)$$

The parameter  $\alpha$  is a characteristic length scale of the bar potential and  $v_0$  is a characteristic circular velocity. The parameter  $\epsilon$  is a free parameter related to the bar strength. Dehnen (2000) used this potential with  $n = 3$  to study the effect of the OLR of the bar of our Galaxy on the local stellar velocity distribution. Fux (2001) uses the same bar potential to model the Galactic bar and to study the order and chaos in the disc. Nevertheless, since the characteristics of the potential with  $n = 3$  are very similar to Ferrers potentials, i.e. the force decreases very abruptly at large radii, we will use here  $n = 0.75$  to avoid this. We will couple this bar with an axisymmetric part given by Eq. 4 and 5 and we will consider three different slopes of the rotation curve in the outer parts, like we did for the previous models. In all three models, the length scale of the bar is set to  $\alpha = 5$  and the circular velocity  $v_0$  is set to 200. The basic value for the corotation radius is set to  $r_L = 6.0$ , and for the bar strength to  $\epsilon = 0.15$  and a range around each of these values

is explored. The spheroid mass is fixed at  $M_{bul} = 3 \times 10^4$ , and the scale length is calculated accordingly. In model R', which has a rising rotation curve, the disc parameters are fixed so that the maximum circular velocity is 164.204 at  $r = 10$ . In model F', which has a flat rotation curve in the outer parts, we fix the values of  $r_d$  and  $V_d$  so that the maximum circular velocity is 164.204 at  $r = 50$ . Model D', which has a decreasing rotation curve in the outer parts, has a maximum disc circular velocity of 164.204 at  $r = 100$ . Results using these models are presented in Sect. 4.3.

We also used in our computations the bar potential given by the expression:

$$\Phi(r, \theta) = \hat{\epsilon} \sqrt{r}(r_1 - r) \cos(2\theta), \quad (8)$$

where  $r_1$  is a characteristic scale length of the bar potential, which we will take for the present purposes to be equal to 20. The parameter  $\hat{\epsilon}$  is related to the bar strength. This type of model has already been widely used in studies of bar dynamics (e.g. Barbanis & Woltjer 1967; Contopoulos & Papayannopoulos 1980; Contopoulos 1981; Athanassoula 1990). We will couple this bar with an axisymmetric part given by Eq. 4 and 5. We will consider two reference models noted with the names of models R'' and D'', again each with a different slope of the rotation curve in the outer parts. The strength parameter is set to  $\hat{\epsilon} = 100$  and the Lagrangian radius is  $r_L = 6$ . The spheroid mass is  $M_{bul} = 3 \times 10^4$ , and the spheroid scale length is calculated accordingly. The disc parameters in model R'' are set so that the maximum disc circular velocity is 164.204 at  $r = 30$ , which corresponds to a rotation curve rising in the outer parts, while for model D'' they are obtained by fixing a maximum circular velocity of 164.204 at  $r = 10$ , which corresponds to a rotation curve falling in the outer parts.

### 3. Invariant manifolds and transfer of matter

In this section, we give a simplified description of the dynamics around the unstable equilibrium points. Readers interested in a more thorough description, in particular of the Lyapunov periodic orbits and of the corresponding invariant manifolds, are referred to Paper I and to references therein. Here, we also define the heteroclinic and homoclinic orbits and describe the role they play in the transfer of matter within the galaxy. We will use these ideas to compare our results with observations in the forthcoming Paper III.

In Sect. 2.1, we mentioned that the equations of motion (Eq. 2) have five equilibrium points, three of which are linearly stable, namely  $L_3$ ,  $L_4$ , and  $L_5$ , and two unstable, namely  $L_1$  and  $L_2$ . Around the equilibrium points there exist families of periodic orbits, e.g. around the central equilibrium point the well-known  $x_1$  family of periodic orbits which is responsible for the bar structure. Around each unstable equilibrium point there also exists a family of periodic orbits, known as the family of Lyapunov orbits (Lyapunov 1949), which, at low energy levels, are unstable and become stable only at high energies (Skokos et al. 2002a). We are interested in this family only in the range of energies where the periodic orbits are unstable. In this range, the size of the periodic orbits remains small and they stay in the vicinity of the equilibrium point. For a given energy level

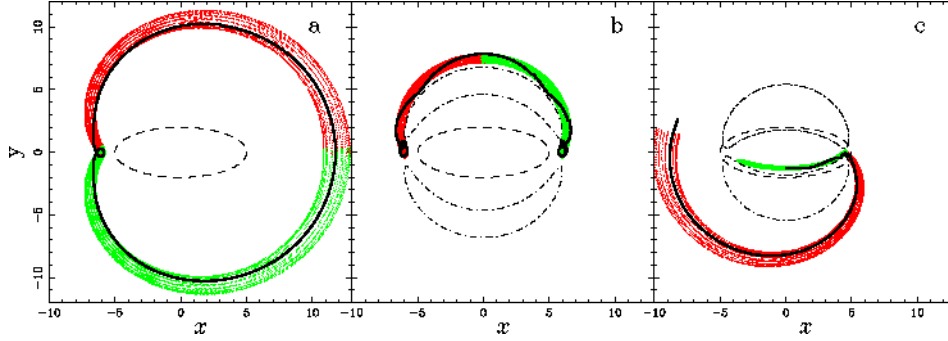


**Fig. 1.** Homoclinic (a), heteroclinic (b) and escaping (c) orbits (black thick lines) in the configuration space. In red lines, we plot the unstable invariant manifolds associated to the periodic orbits, while in green we plot the corresponding stable invariant manifolds. In dashed lines, we give the outline of the bar and, in (b) and (c), we plot the zero velocity curves in dot-dashed lines.

within this range, two stable and two unstable sets of asymptotic orbits emanate from the periodic orbit and they are known as the stable and unstable invariant manifolds, respectively. We denote by  $W_{\gamma_i}^s$  the stable invariant manifold associated to the periodic orbit  $\gamma$  around the equilibrium point  $L_i$ ,  $i = 1, 2$ . This stable invariant manifold is the set of orbits that tends to the periodic orbit asymptotically. In the same way we denote by  $W_{\gamma_i}^u$  the unstable invariant manifold associated to the periodic orbit  $\gamma$  around the equilibrium point  $L_i$ ,  $i = 1, 2$ . This unstable invariant manifold is the set of orbits that departs asymptotically from the periodic orbit (i.e. orbits that tend to the Lyapunov orbits when the time tends to minus infinity). Since the invariant manifolds extend well beyond the neighbourhood of the equilibrium points, they can be responsible for global structures.

In our planar model, the dynamics take place in a four dimensional phase space. In fact, the number of dimensions can be reduced by one by fixing the energy to the energy level of the Lyapunov periodic orbit. In this three dimensional space, the stable and unstable invariant manifolds associated to a Lyapunov orbit are sets of asymptotic trajectories that form tubes. These tubes are filled and surrounded by a bundle of trajectories (see Fig 5 of Paper I, and Gómez et al. 2004 and references therein for more details). A good way to visualise these tubes and make use of them is by means of Poincaré surfaces of section, this is, by drawing the crossings of the trajectories through a particular plane, or surface in phase space. Depending on the purposes of our study, some surfaces will be more suitable than others, but the methodology is the same. Let us take as an example the surface of section  $\mathcal{S}$  defined by  $y = 0$  with  $x > 0$ , this is, we consider the orbits when they cut the plane  $y = 0$  having a positive value for the  $x$  coordinate. Let us consider this surface of section  $\mathcal{S}$  for the stable and unstable invariant manifolds of a Lyapunov orbit around  $L_2$  (located in the  $x < 0$  side). Taking initial conditions close to the Lyapunov orbit and integrating  $W_{\gamma_2}^u$  forward in time (resp.  $W_{\gamma_2}^s$  backwards in time) until the first encounter with  $\mathcal{S}$  we obtain the simple closed curves  $W_{\gamma_2}^{u,1}$  (resp.  $W_{\gamma_2}^{s,1}$ ) which can be seen in Figs. 2 and 3 that will be commented later. In Fig. 1a we can also see the plot of the trajectories until the encounter with  $\mathcal{S}$ . Although the simple closed curves  $W_{\gamma_2}^{u,1}$  and  $W_{\gamma_2}^{s,1}$  are obtained as the natural result of intersecting the manifold tubes with a plane, it should be mentioned that further crossings (i.e.  $W_{\gamma_2}^{u,k}$  and  $W_{\gamma_2}^{s,k}$

with  $k > 1$ ) may well not have this simple structure, as can be seen in Gidea and Masdemont (2007).

In the selected example,  $W_{\gamma_2}^{u,1}$  and  $W_{\gamma_2}^{s,1}$  are represented in  $(x, \dot{x})$  coordinates. It is important to note that a pair  $(x, \dot{x})$  in  $\mathcal{S}$  defines an orbit in a unique way, since  $y = 0$  and  $\dot{y}$  is obtained from the energy level under study. By the definition of an invariant manifold, a point in  $W_{\gamma_2}^{u,1} \cap W_{\gamma_2}^{s,1}$  represents a trajectory asymptotic to the Lyapunov orbit  $\gamma$  around  $L_2$  both forward and backward in time. It is called an homoclinic orbit. In general, homoclinic orbits correspond to asymptotic trajectories,  $\psi$ , such that  $\psi \in W_{\gamma_i}^u \cap W_{\gamma_i}^s$ ,  $i = 1, 2$ . Thus, a homoclinic orbit departs asymptotically from the unstable Lyapunov periodic orbit  $\gamma$  around  $L_i$  and returns asymptotically to it (see Fig. 1a). Heteroclinic orbits, on the other hand, are defined as asymptotic trajectories,  $\psi'$ , such that  $\psi' \in W_{\gamma_i}^u \cap W_{\gamma_j}^s$ ,  $i \neq j$ ,  $i, j = 1, 2$ . Thus, a heteroclinic orbit departs asymptotically from the periodic orbit  $\gamma$  around  $L_i$  and approaches asymptotically the corresponding Lyapunov periodic orbit with the same energy around the Lagrangian point at the opposite end of the bar  $L_j$ ,  $i \neq j$  (see Fig. 1b; a suitable surface of section for this computation can be the plane  $x = 0$ ).

In our computations we also consider the overlap area corresponding to *homoclinic* orbits as the area resulting from the intersection of the interior regions of  $W_{\gamma_i}^{u,1}$  and  $W_{\gamma_i}^{s,1}$ ,  $i = 1, 2$  (see Fig. 3). Analogously, we define the overlap area corresponding to *heteroclinic* orbits as the area resulting from the intersection of the interior regions of  $W_{\gamma_i}^{u,1}$  and  $W_{\gamma_j}^{s,1}$ ,  $i \neq j$ ,  $i, j = 1, 2$ .  $W_{\gamma_i}^{u,1}$  and  $W_{\gamma_j}^{s,1}$  for a given model and energy may or may not intersect and, as the parameters of the model change, they can approach each other or move away. For instance, Fig. 2 shows the curves  $W_{\gamma_2}^{u,1}$  and  $W_{\gamma_2}^{s,1}$  on the plane  $\mathcal{S}$  for our model F, introduced in Sect. 4.2, for four different values of the quadrupole moment  $Q_m$ . We note that models with nonzero intersection of  $W_{\gamma_i}^{u,1}$  and  $W_{\gamma_i}^{s,1}$  are not associated to isolated values of the given free parameter (in our example  $Q_m$ ), but they define a range. So we will find trajectories that depart asymptotically from the periodic orbit, follow  $W_{\gamma_i}^u$  and do not intersect the corresponding stable invariant manifold in phase space. These trajectories initially spiral out from the region of the unstable periodic orbit (see Fig. 1c) and we refer to them as escaping trajectories.

We will argue in Paper III that these three types of orbits – namely, the homoclinic, the heteroclinic, and the escaping orbits – become the backbone of ringed structures and of spiral arms observed in disc galaxies and we will follow how the overlap area gives a measure of these behaviours.

## 4. Results

The next subsections are devoted to the results obtained when we vary the parameters of the models introduced in Sect. 2.2. In order to best see the influence of each parameter separately, we make families of models in which only one of the free parameters is varied, while the others are kept fixed. We start by studying the effects of the main four parameters of model A. We then study the effect of having reference models with a Ferrers bar potential and rising, flat, or falling rotation curves in the outer parts. Finally, we study the effects of having bar potentials with a larger influence in the outer parts.

### 4.1. Model A. The effect of the main four parameters

In this section we study the effect of the variation of the parameters of model A on the shape of the invariant manifolds. We consider both homogeneous ( $n = 0$ ) and inhomogeneous ( $n = 1$ ) Ferrers bar models (Eq. 6). The main four parameters are the axial ratio of the bar,  $a/b$ , the Lagrangian radius,  $r_L$ , the quadrupole moment,  $Q_m$ , and the central concentration,  $\rho_c$ . For all four, we will take the same range of values as in Athanassoula (1992a), since it is wide enough to make sure we cover all relevant values. According to Kormendy (1982), typical bar axial ratios range from 2.5:1 to 5:1, while ovals have considerably smaller axial ratios. We thus choose values of the axial ratio within the range  $a/b = 1.2 - 6$ . As the rings and spirals generally emanate from the ends of bars, the unstable Lagrangian points should be placed in the vicinity of the bar end points, which are at  $x = \pm 5$ . We let the parameter  $r_L$  vary accordingly within the range  $r_L = 3.5 - 8.5$ , i.e. we consider Lagrangian points placed from well within the bar up to well beyond the bar end points. The values for the quadrupole moment are chosen within the range  $Q_m = 0.1 \times 10^4 - 12 \times 10^4$ , covering all the range from weak bars or ovals to very strong bars. Finally, the central concentration is related to the presence of the spheroid. In this set of models the central concentration is varied within the range  $\rho_c = 0.02 \times 10^4 - 3.6 \times 10^4$ . For a given value of the bar central density, higher values of  $\rho_c$  indicate denser bulges. We used two values of the concentration index of the bar, namely  $n = 0$  and  $n = 1$ . For each of these indexes, we make families of models in which just one of the free parameters is varied, while the others are kept fixed. We use these families to study the influence of each of the free parameters on the global shape of the invariant manifolds.

In Fig. 5 we show the effect of the four free parameters on the shape of the invariant manifolds for model A with  $n = 0$ . In each panel, we plot the outline of the bar and, for a given energy level, the unstable invariant manifolds associated to the Lyapunov orbits of both  $L_1$  and  $L_2$  equilibrium points, integrated until they perform half a revolution. For initial conditions of the invariant manifolds very near the Lyapunov orbit,

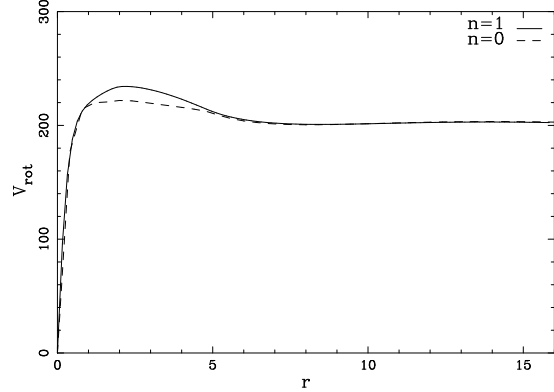


**Fig. 4.** Rotation curves corresponding to model A for  $n = 0$  (dashed line) and  $n = 1$  (solid line).

this time corresponds in all cases to approximately 3 bar rotations, i.e. to  $\sim 0.25$  Gyr. In columns 1 to 4 we show the effect of the bar axial ratio (first column), of the Lagrangian radius (second column), of the quadrupole moment (third column) and of the central concentration (fourth column). In all columns the numerical values of the parameters increase from top to bottom. Results for  $n = 1$  are very similar, so we do not show them here.

Fig. 5 shows that the central concentration has hardly any influence on the shape of the invariant manifolds, which corresponds in all cases to the morphology of an  $rR_1$  ringed galaxy. From the ends of the bar emanate branches that curl around the bar until the opposite end, forming two rings. One ring is close to the bar and is elongated along it, but not far from circular, i.e. has the location and properties of observed inner rings. The other ring is at larger radii and is elongated perpendicularly to the bar major axis, i.e. it has the location and properties of an outer ring  $R_1$ . This description also holds for all values of the bar axial ratio. Varying this quantity has hardly any influence on the outline of the outer branches of the invariant manifolds, but does have some, albeit small, on the inner ones. Namely, for  $a/b = 1.2$ , the inner ring is near-circular, while for larger values it is diamond shaped.

On the contrary, varying the value of  $r_L$  introduces different morphologies. When the Lagrangian points are well within the bar, the inner ring is also within the bar, which is not realistic. The outer ring is not closed, i.e. we have a spiral. However, this spiral also is not realistic, because it does not emanate from the ends of the bar. For values of the Lagrangian radius beyond  $r_L = 5$ , the outer branches of the invariant manifolds tend to the opposite ends of the bar, and when they close they form an outer ring. Thus, the morphology is again that of an  $rR_1$  ringed galaxy. As  $r_L$  increases, the inner ring increases in size and becomes more circular. Already for  $r_L = 6.5$  the inner ring size is considerably larger than the bar, contrary to what is observed. For the highest of the considered values, the inner ring forms a nearly circular structure with about double the size of the bar.

Finally, the variation of the bar strength also gives different shapes of the ringed structures. In the case of weak bars, i.e. small  $Q_m$  values, the inner ring is nearly circular with a diam-

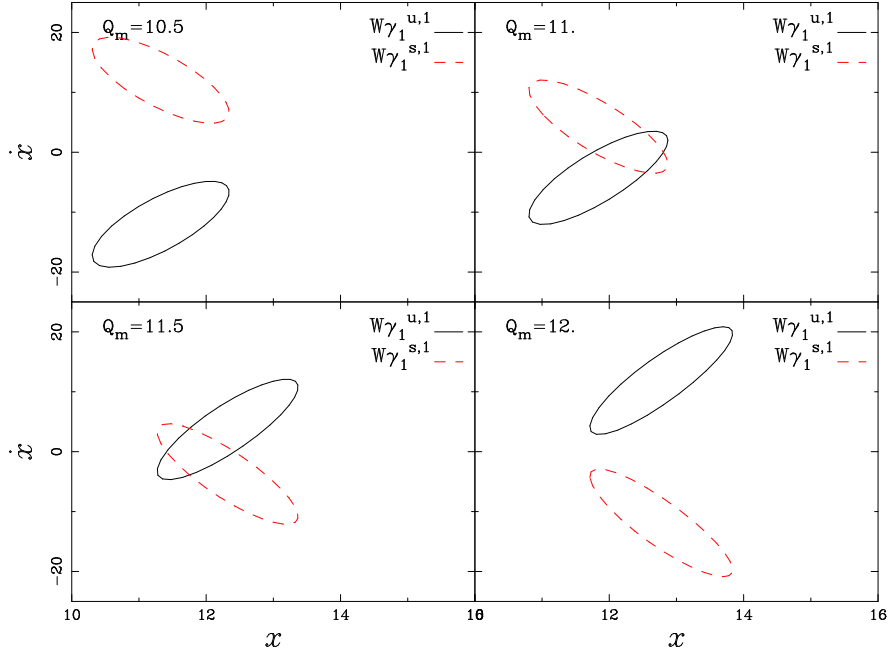


**Fig. 2.** Evolution of the curves  $W_{\gamma_2}^{u,1}$  (black solid lines) and  $W_{\gamma_1}^{s,1}$  (red dashed line) on the phase space  $x\dot{x}$  for a particular galactic model and four values of  $Q_m$  (given in the upper left corner of each panel in units of  $10^4$ ).

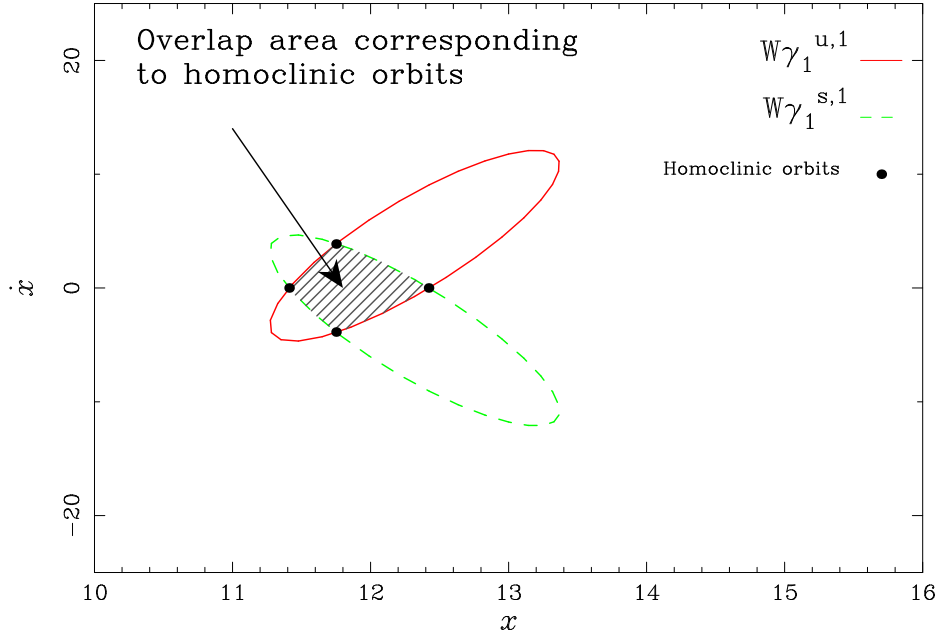


**Fig. 3.** Definition of the overlap area corresponding to homoclinic orbits. The curves  $W_{\gamma_2}^{u,1}$  (in red solid line) and  $W_{\gamma_2}^{s,1}$  (in green dashed line) intersect on the plane  $(x, \dot{x})$ . The four black points correspond to homoclinic orbits, while the hatched area is the overlap area corresponding to homoclinic orbits.

eter about the size of the bar. However, as will be discussed in paper III, the outline is not that of an  $rR_1$  ringed galaxy. As the quadrupole moment increases and the bar gets stronger, the inner ring becomes more elongated along the bar until, for the case of strong bars, it is deformed in shape. The outer ring gets bigger in size with increasing  $Q_m$ , so that the ratio between the ring diameters increases. In the case of strong bars, both the inner and outer rings become asymmetric with respect to the

major and minor axes of the bar and their major and minor diameters do not coincide any more with the  $x$  and  $y$  axes.

We can therefore conclude that the shape of the invariant manifolds is not sensitive to the variation of the axial ratio and of the central density. On the other hand, when we vary the Lagrangian radius or the quadrupole moment, we obtain richer structures. These differences are related to the values of the effective potential of the models. This can be seen in Fig. 6,

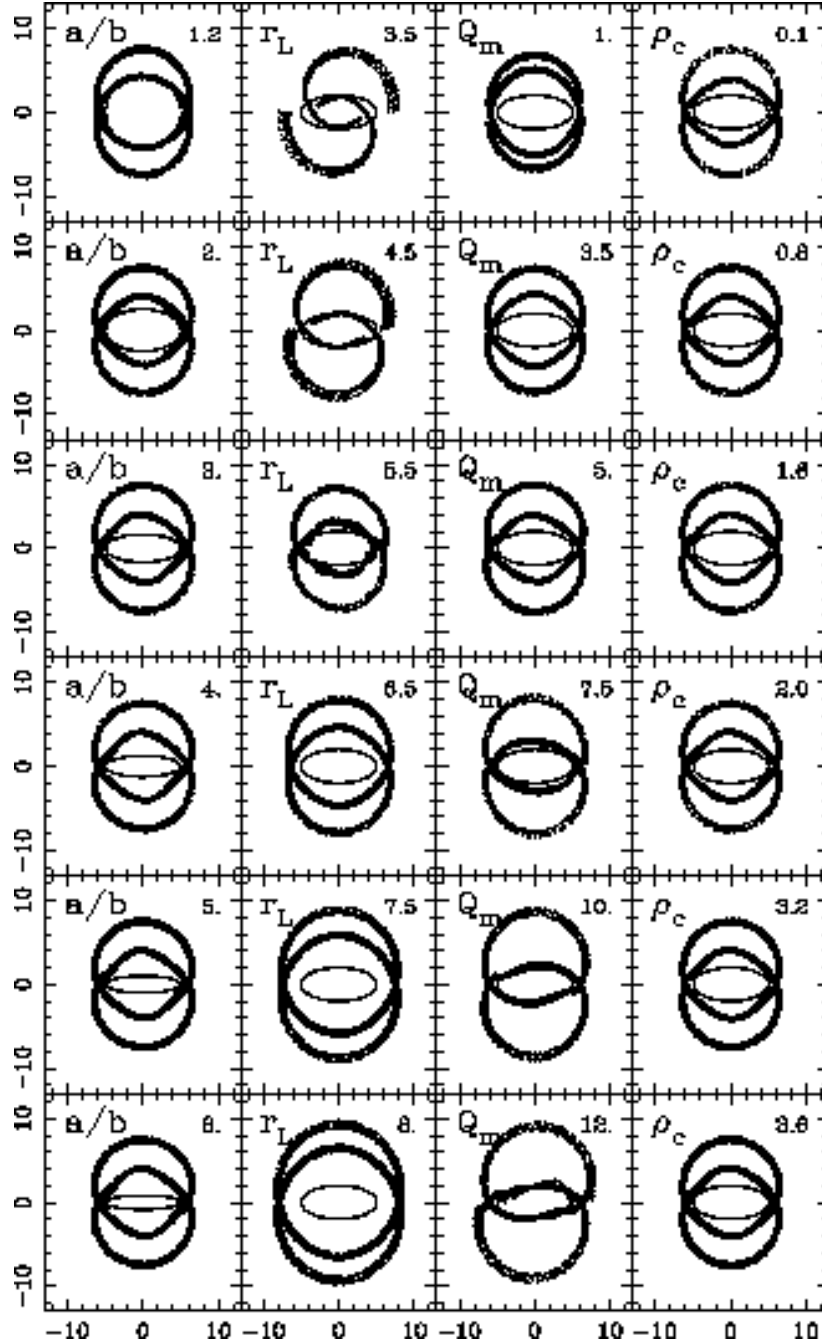


**Fig. 5.** Ring and spiral structures in four sequences of models with  $n = 0$  and various values of the four main parameters (given in the upper corners of each panel). For the remaining parameters, see text. *First column:* effect of the variation of the axial ratio of the bar,  $a/b$ ; *Second column:* effect of the variation of the Lagrangian radius,  $r_L$ ; *Third column:* effect of the variation of the quadrupole moment,  $Q_m$  (in units of  $10^4$ ); *Fourth column:* effect of the variation of the central density,  $\rho_c$  (in units of  $10^4$ ). In all panels, we plot on the  $x - y$  plane the outline of the bar (thin solid line) and the unstable invariant manifolds associated to the Lyapunov orbits for a given energy level.

where we plot the effective potential of the models along the bar major axis. First, we note that for radii smaller than the length of the bar, the effective potential shows some differences in all the cases. This means that all four free parameters will have an effect in the interior structure of the bar and is in agreement with the fact that both the orbital structure and the gas flow in the bar region vary considerably as the values of the four main parameters are changed (Athanasoula 1992a, 1992b). Here,

however, we are interested in the spirals and rings which occur in a region from the ends of the bar outwards. For radii larger than the length of the bar, the effective potential depends little on the value of the axial ratio, or of the central concentration. This is illustrated in Fig. 6a and Fig. 6c for homogeneous and inhomogeneous bars, respectively. On the other hand, when we vary the Lagrangian radius or the quadrupole moment, the effective potential is considerably influenced. This is shown in



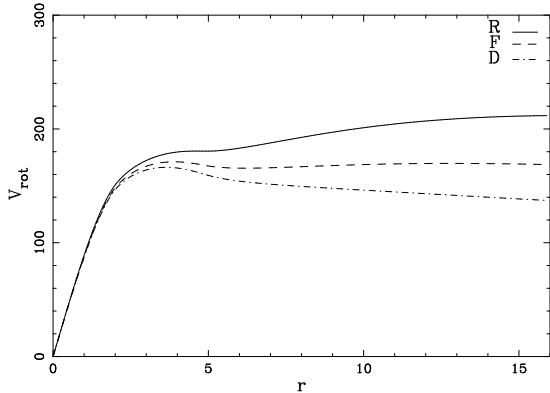


**Fig. 7.** Rotation curves corresponding to models R (solid line), F (dashed line) and D (dot-dashed line). Note that all models have the same rotation curve slope in the inner parts.

Fig. 6b and Fig. 6d, again for homogeneous and inhomogeneous bars, respectively. This explains why only the variation of the Lagrangian radius and of the quadrupole moment has an effect on the global shape of the invariant manifolds.

#### 4.2. Models R, F and D. The effect of having a rising, flat, or falling rotation curve with a Ferrers ellipsoid

In general, rotation curves in the outer parts of disc galaxies are flat (Bosma 1981). However, many cases of slightly rising or slightly falling rotation curves are known. We thus want to study the possible influences of these different rotation curves shapes on the morphological structure of our models.

In this section we use reference models R, F and D, each having a different slope of the rotation curve in the outer parts. The rotation curves of these models are shown in Fig. 7. Note that in all cases the slope of the inner parts is the same, while in the outer parts it is rising (model R), flat (model F), or decreasing (model D). For each of these reference models we generate families of models, where we vary only one of the free parameters. Since in Sect. 4.1 we showed that the whole range of two of the main parameters corresponds to the same morphology and dynamics beyond the bar region, and explained the reason for this, here we will study only the effect of the variation of the two crucial parameters, namely the values of  $r_L$  and  $Q_m$ . The range of variation of these parameters will be the same as in Sect. 4.1, i.e.  $r_L = 3.5 - 8.5$  and  $Q_m = 0.5 \times 10^4 - 12 \times 10^4$ , while the values of  $\rho_c$  and  $a/b$  are kept fixed to  $0.05 \times 10^4$  and 2.5, respectively.

In Fig. 8 we show the effect of the variation of the Lagrangian radius on the shape of the invariant manifolds. In all columns we increase the value of  $r_L$  from top to bottom, while the value of the quadrupole moment is fixed to  $Q_m = 4.5 \times 10^4$ . We note that, for rotation curves which in the outer parts are rising or flat, the shape of the invariant manifolds presents the same behaviour as in model A (see previous subsection). Thus, for small  $r_L$  values we have spiral arms, while for large  $r_L$  values we have outer rings. An inner ring is present in all cases and its size increases with  $r_L$ . It is smaller than the bar, i.e. unrealistic, for  $r_L < a$  and much larger than the bar, i.e. again

unrealistic, for very large  $r_L$  values, while realistic sizes are only found for an intermediate range of values. In the case of falling rotation curves, the evolution is similar. However, when the Lagrangian radius is close to the bar length, the invariant manifolds cross each other, forming an  $R_2$  ring.

Along each row we observe the effect of changing the slope of the rotation curve at the outer radii, while keeping constant the value of all bar parameters, including the corotation radius. In the upper row, where the Lagrangian points are inside the bar, the spiral arms open as the slope of the rotation curve decreases. A case where corotation is near the ends of the bar is shown in the second row. A rising rotation curve gives an  $rR_1$  ring, while a flat rotation curve gives a  $R_1$  pseudo-ring. In the specific case of a falling rotation curve, the outer branches of the invariant manifolds are long and open, finally crossing each other, thus forming an  $R_2$  ring. For values of the corotation radius beyond the end of the bar, the shape corresponds to that of an  $rR_1$  ring galaxy.

In Fig. 9, we show the effect of the variation of the quadrupole moment on the shape of the invariant manifolds. In all columns we increase the value of  $Q_m$  from top to bottom, while the value of the Lagrangian radius is fixed to  $r_L = 6$ . In the case of reference models with rising or flat rotation curves (first and second columns), the behaviour of the invariant manifolds is the same as in model A. For a falling rotation curve and a weak bar, we still have an  $rR_1$  ring structure. As we increase the bar strength, first the inner ring becomes distorted, then the major axis of the outer ring ceases to be perpendicular to the bar major axis, and finally, with strong bars, the outer invariant manifolds either do not close and form spiral arms, or they are long and cross each other, thus forming  $R_2$  rings. As in the previous figure, along each row we observe the effect of changing the slope of the rotation curve in the outer parts, while keeping constant the bar quadrupole moment. For weak and intermediate strength bars, the shape of the rotation curve does not influence the morphology. For strong bars, however, we obtain different structures. A rising rotation curve gives an  $rR_1$  ring, while a flat rotation curve gives an asymmetric ring. In the case of falling rotation curves, the outer branches of the invariant manifolds are open and form spiral arms and  $R_2$  rings.

#### 4.3. Models R', F' and D'. Other bar models

As previously mentioned, Ferrers ellipsoids do not have a great influence in the outer region, which is where the outer branches of the invariant manifolds are found. Since we argue in this paper that invariant manifolds are responsible for the rings and spiral structures, we considered also bar potentials of either of Dehnen type (Eq. 7), or of Barbanis-Woltjer type (Eq. 8). The results of the two models are, however, very similar, so for the sake of brevity we discuss only the results for the Dehnen type bar here. In this case we use models R', F' and D', again each with a different slope of the rotation curve in the outer parts. The rotation curves of these models are shown in Fig. 10. As in the previous sections, we make families of models, varying one of the parameters, while keeping the rest constant. Since these models are ad hoc and they do not correspond to

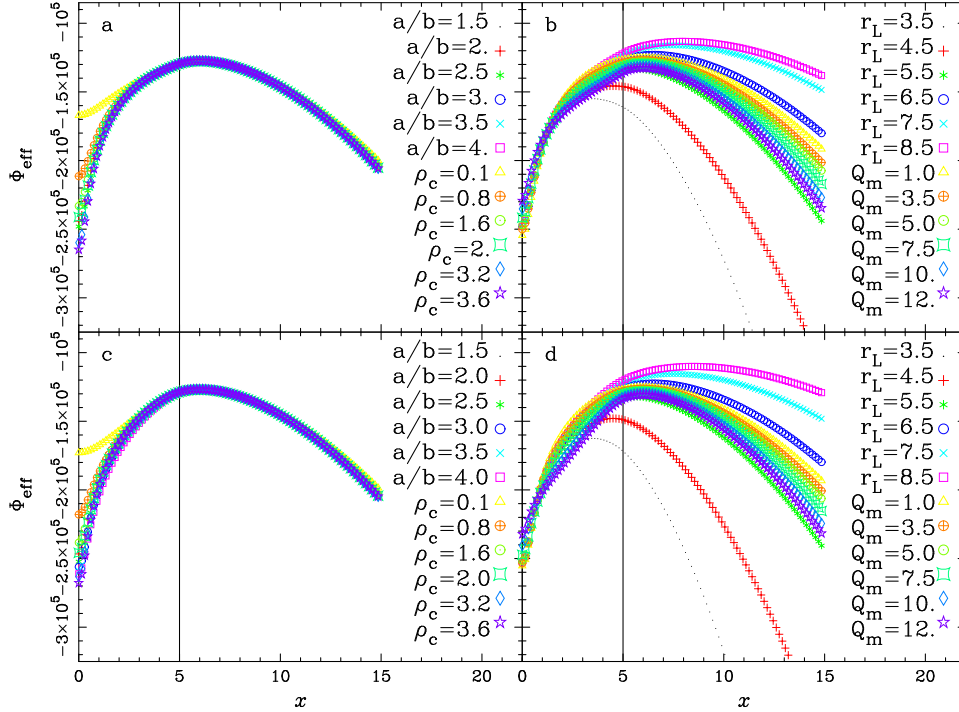


**Fig. 6.** Effective potential along the bar semi-major axis for model A with  $n = 0$  and  $n = 1$ . **(a)** Models with homogeneous ( $n = 0$ ) bars with different values of the bar axial ratio,  $a/b$ , and of the central density  $\rho_c$  (in units of  $10^4$ ). **(b)** Models with homogeneous bars ( $n = 0$ ) with different values of the Lagrangian radius,  $r_L$ , and of the quadrupole moment,  $Q_m$  (in units of  $10^4$ ). **(c)** Same as in **(a)** but with inhomogeneous bars ( $n = 1$ ). **(d)** Same as in **(b)** but with inhomogeneous bars ( $n = 1$ ). The solid vertical line marks the end of the bar.

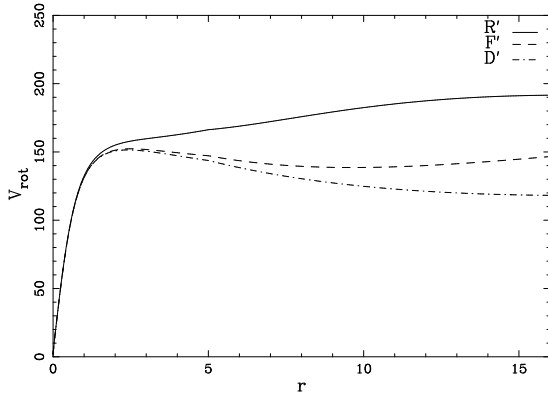


**Fig. 10.** Rotation curves corresponding to models R' (solid line), F' (dashed line) and D' (dot-dashed line). Note that all models have the same rotation curve slope in the inner parts.

any simple and realistic density, choosing the parameters is less easy, since there are less constraints from observations. Based on the results of Sect. 4.1, we use as free parameters only the Lagrangian radius,  $r_L$ , and  $\epsilon$ , which determines the bar strength. The values of  $r_L$  are taken within the range  $r_L = 3.5 - 8.5$ , as in the previous sections. The values of  $\epsilon$  are taken within the range  $\epsilon = 0.01 - 0.3$ , which corresponds a range of 5 to 26% for the ratio of the non-axisymmetric component to the axisymmetric component of the force in the  $x$ -direction and at the radius  $r = 16$ .

In Fig. 11 we show the effect of the Lagrangian radius on the shape of the invariant manifolds. In all columns we increase the value of  $r_L$  from top to bottom, while the strength parameter  $\epsilon$  is fixed to 0.15. For model R', i.e. for a rotation curve which is slightly increasing, we start at the smallest  $r_L$  with a spiral. As the value of  $r_L$  is increased the spiral gets more tightly wound and then closes forming a somewhat asymmetric outer ring. These changes are accompanied by an increase of the size of the inner ring, which, nevertheless, is in all cases quite asymmetric. For model D', i.e. for a somewhat decreasing rotation curve, at the smallest  $r_L$  value we have a rather open spiral. As the value of  $r_L$  is increased, the extent of the spiral increases considerably and its pitch angle increases slightly. For the largest  $r_L$  value,  $r_L = 8.5$ , the outer branches of the stable and unstable invariant manifolds delineate well the loci of both types of outer rings, namely  $R_1$  and  $R_2$ , thus forming an  $R_1R_2$  ring. The inner ring also increases in size as the value of  $r_L$  increases, while staying of roughly the same shape. The position angle leads that of the bar by an angle which, as we increase  $r_L$ , increases approximately from 20 to 36 degrees. The sequence with the flat rotation curve, F', is the richest in morphological types. It starts with a rather open spiral, as the D' sequence, but, contrary to the D', the shape of the invariant manifold branches changes considerably. Thus, for the largest  $r_L$  value they form asymmetric outer and inner rings, similar in outline to those formed for model R' and  $r_L = 4.5$ . In between these two, the invariant manifolds give us two different morphologies. For  $r_L = 4.5$ , the outer branches of the stable and

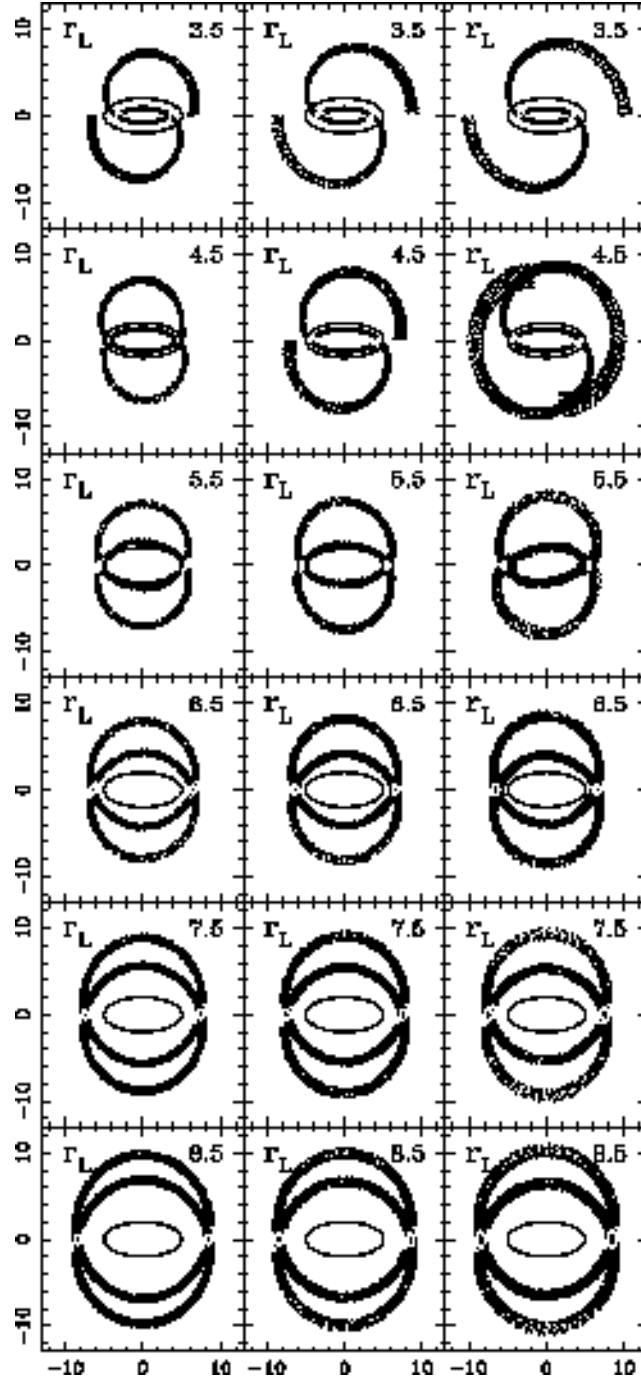


**Fig. 8.** Rings and spirals for three sequences of models with reference models R (left), F (middle) and D (right) where we vary the Lagrangian radius,  $r_L$ . This value increases from top to bottom and is given in the upper right corner of each panel. The value of the quadrupole moment is fixed to  $Q_m = 4.5 \times 10^4$ . In all panels, we plot on the  $x - y$  plane the outline of the bar (thin solid line), the two unstable Lyapunov orbits associated to the unstable equilibrium points  $L_1$  and  $L_2$  (white solid line), and the unstable invariant manifolds associated to the Lyapunov orbits, all for a given energy level.

unstable invariant manifolds outline the shape of  $R_1R_2$  rings, as for model D' and  $r_L = 8.5$ , while the inner ring is deformed in shape. For  $r_L = 5.5$ , the outer branches of the unstable invariant manifolds evolve until they cross each other forming an outer ring whose principal axis is parallel to the bar major axis, thus forming an  $R_2$  outer ring.

In each row we observe the effect of keeping constant the value of corotation radius and of all other bar parameters, while changing the slope of the rotation curve at outer radii. When the Lagrangian radius is smaller than the bar length, the spiral arms open as the slope of the rotation curve decreases. The case where corotation is approximately the value of the bar length scale is shown in the second row. A rising rotation curve gives

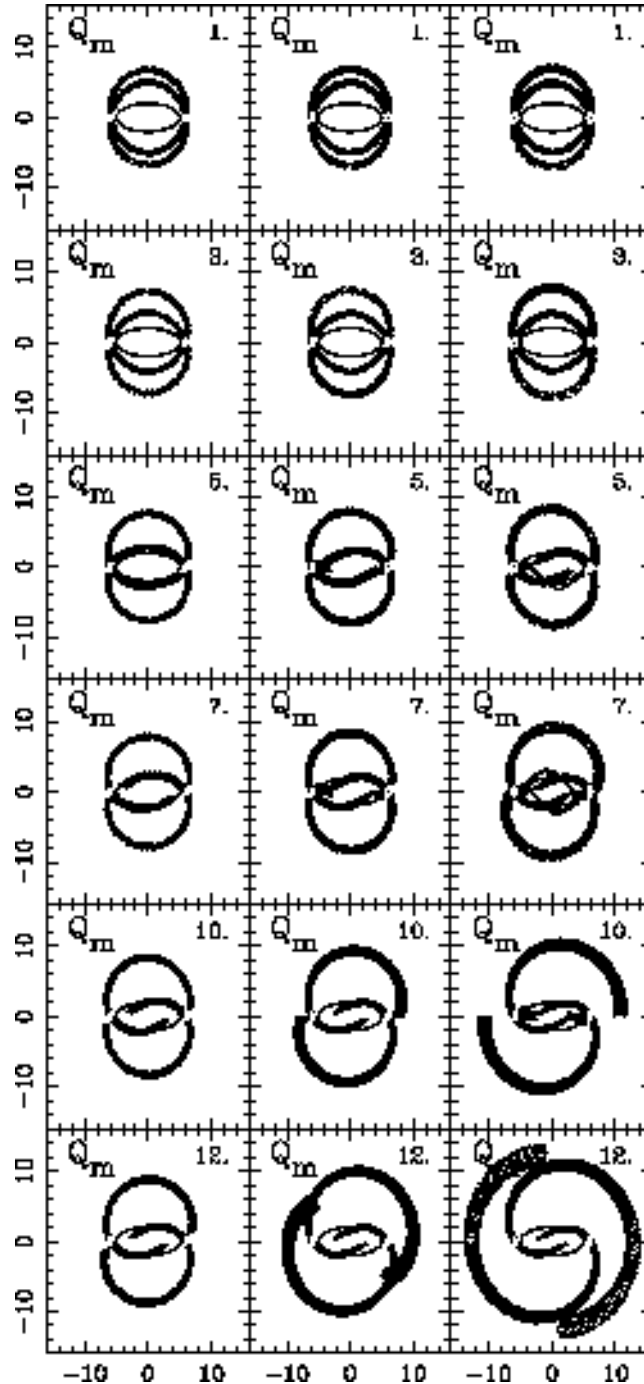


**Fig. 9.** Same as in Fig. 8, for three sequences of models with reference models R (left), F (middle) and D (right) and different values of the quadrupole moment,  $Q_m$ , given in units of  $10^4$  in the upper right corner of each panel. The value of the Lagrangian radius is fixed to  $r_L = 6$ .

a broken and misaligned  $rR_1$  ring, while a flat rotation curve gives  $R_1R_2$  rings, and a falling rotation curve gives spiral arms. The tendency is similar if the values of the Lagrangian radius are somewhat larger than the bar length scale. For a rising rotation curve, the structure of the galaxy is that of an  $rR_1$  ring. However, if the rotation curve is flat, we obtain  $R_2$  rings, while if the rotation curve is falling, we obtain spiral arms. As we increase the value of the Lagrangian radius further, the invariant manifolds tend to approach the opposite ends finally forming

outer rings misaligned with respect to the bar. The inner rings, in turn, tend to open as the Lagrangian radius increases. In the case of a falling rotation curve, the invariant manifolds form spiral arms.

In Fig. 12, we show the effect of the bar strength on the shape of the invariant manifolds. In all columns we increase the value of  $\epsilon$  from top to bottom, while the value of the Lagrangian radius is fixed to  $r_L = 6$ . In the case of reference models with a rising rotation curve, the invariant manifolds tend to open.

Thus, we have a behaviour opposite to the one we found when we increased the value of the Lagrangian radius. That is, for low values of the parameter  $\epsilon$ , the galaxy morphology is that of an  $rR_1$  ring, while as the bar strength increases, the branches of the invariant manifolds tend to open and form spiral arms. The inner ring is, for low values of  $\epsilon$ , symmetric. As the bar strength increases, it becomes more eccentric and finally asymmetric. For a flat rotation curve and a weak bar, we initially have an  $rR_1$  ring structure. As we increase the bar strength, the inner ring becomes distorted, while the major axis of the outer ring ceases to be perpendicular to the bar major axis. Increasing the bar strength, we find spirals. A further increase of the bar strength brings a morphology of the  $R_1R_2$  type (see middle panel for  $\epsilon = 0.2$ ) and then (see middle panel for  $\epsilon = 0.25$ ) a morphology of the  $R_2$  type. Finally, with strong bars the outer invariant manifolds do not close, thus forming spiral arms. For a falling rotation curve, the behaviour is similar to the F' case but the invariant manifolds become open for weaker bars. As the bar strength increases, the outer branches of the invariant manifolds open forming  $R_1R_2$  rings and spiral arms, but the inner branches will appear distorted.

In each row, we observe the effect of changing the slope of the rotation curve in the outer parts. For weak bars, the invariant manifolds tend to open as the slope of the rotation curve decreases. Note that this behaviour is similar to the one obtained for keeping constant the value of corotation radius. We obtain  $R_1R_2$  rings for weak bars and falling rotation curves or intermediate strength bars and flat rotation curves. In the case of strong bars, the morphologies obtained are spiral arms and  $R_2$  rings.

## 5. Summary and discussion

In this paper we developed an idea originally proposed in Paper I, namely that spirals and rings in barred galaxies can be explained in a common dynamical framework. This is based on the dynamics of the unstable equilibrium points in the rotating bar potential and, more specifically, on the invariant manifolds associated to the unstable Lyapunov periodic orbits around these equilibrium points. These unstable Lyapunov orbits are simple orbits of elliptical-like shape, encircling one of the unstable equilibrium points and staying always in its immediate vicinity. The dynamics of the corresponding manifolds have been well studied by orbital structure theory and we have drawn heavily from that field for our purposes. It is not, however, necessary to master the intricacies of the definition and dynamics of invariant manifolds in order to follow our work. The reader may simply think of a set (a bundle) of orbits emanating from the vicinity of the Lyapunov orbits, i.e. from nearby positions and velocities.

We investigated different barred galaxy models, to make sure that none of our principal results are model dependent and also in order to give ourselves a broad base to allow us, in Paper III, to discuss globally the application of our results to real galaxies. Model A is identical to that introduced by Athanassoula (1992a). Models R, F and D are similar, but allow for rotation curves which can be slightly rising (R), flat (F), or decreasing (D). Finally, Models R', F' and D' (or R''

and D'') are similar to R, F and D, but have a Dehnen-type (or a Barbanis-Woltjer type) bar.

Our main result is that the loci outlined by the invariant manifolds and by the orbits associated with them can reproduce, for appropriate values of the model parameters, all the morphologies observed in real galaxies. Thus we can obtain two spiral arms emanating from the ends of the bar, or rings. We obtain inner rings as well as all the varieties of outer rings, namely  $R_1$ ,  $R_2$  and  $R_1R_2$ . This is shown in Fig. 13, where we show one typical example of each kind of morphology. These include an  $rR_1$  morphology (Fig. 13a) as in NGC 2665 (Buta & Crocker 1991), an  $rR_2$  one (Fig. 13b) as in ESO 325 - 28 (Buta & Crocker 1991), an  $R_1R_2$  one (Fig. 13c) as in NGC 3081 (Buta & Purcell 1998; Buta, Byrd & Freeman 2004), and a spiral (Fig. 13d) as in NGC 1365 (Jörsäter & Moorsel 1995). It is important to stress that all these types were obtained with the *same* dynamics. Indeed, all that differs between these four examples is the values of the model parameters and the bar model potential.

Model A has four basic free parameters describing the bar dynamics. We show that two of these, the bar axial ratio and the central concentration of the model, hardly influence the loci of the invariant manifolds, while the two others, namely the Lagrangian radius and the bar quadrupole mass, have a considerable effect. We explain this by looking at the influence of these four parameters on the effective potential of the system. The main type of morphology found in model A is the  $rR_1$  type. Allowing for different slopes of the rotation curve and/or different bar models, we introduce the remaining morphological varieties.

In this paper we considered a very large number of models and of model parameters and calculated in all cases the appropriate invariant manifolds in order to find the resultant morphology. This can also be applied to real galaxies. Using an image of the galaxy in the near infrared and with an estimate of the thickness and of the mass-to-light ratio, one can obtain the bar potential. Including information from the rotation curve, one can obtain the total potential in which the manifolds and orbits can be calculated. A similar procedure has been already applied e.g. by Lindblad, Lindblad & Athanassoula (1996) to study the gas flow in NGC 1365 and by Byrd, Buta & Freeman (2006) to study the rings of NGC 3081. The latter work in particular studies the shape of the inner and outer rings both analytically and with the help of simulations. Of course, as is the case for all modelling of observations, e.g. concerning the mass-to-light ratios and the thickness, this procedure relies on a few approximations and assumptions. Yet it has revealed a lot of important information on bars and spirals (e.g. Sanders & Tubbs 1980; Duval & Athanassoula 1983; Lindblad, Lindblad & Athanassoula 1996; Patsis, Athanassoula & Quillen 1997; Weiner, Sellwood & Williams 2001; Kranz, Slyz & Rix 2003; Perez, Fux & Freeman 2004; Byrd, Buta & Freeman 2006) and would thus be well worth pursuing for the model presented here.

This paper leaves two major points unanswered. The first one is why a given set of model parameters gives a given morphology? Our work so far shows that this is not a random process, but does not explain the physics behind it. Thus we are not

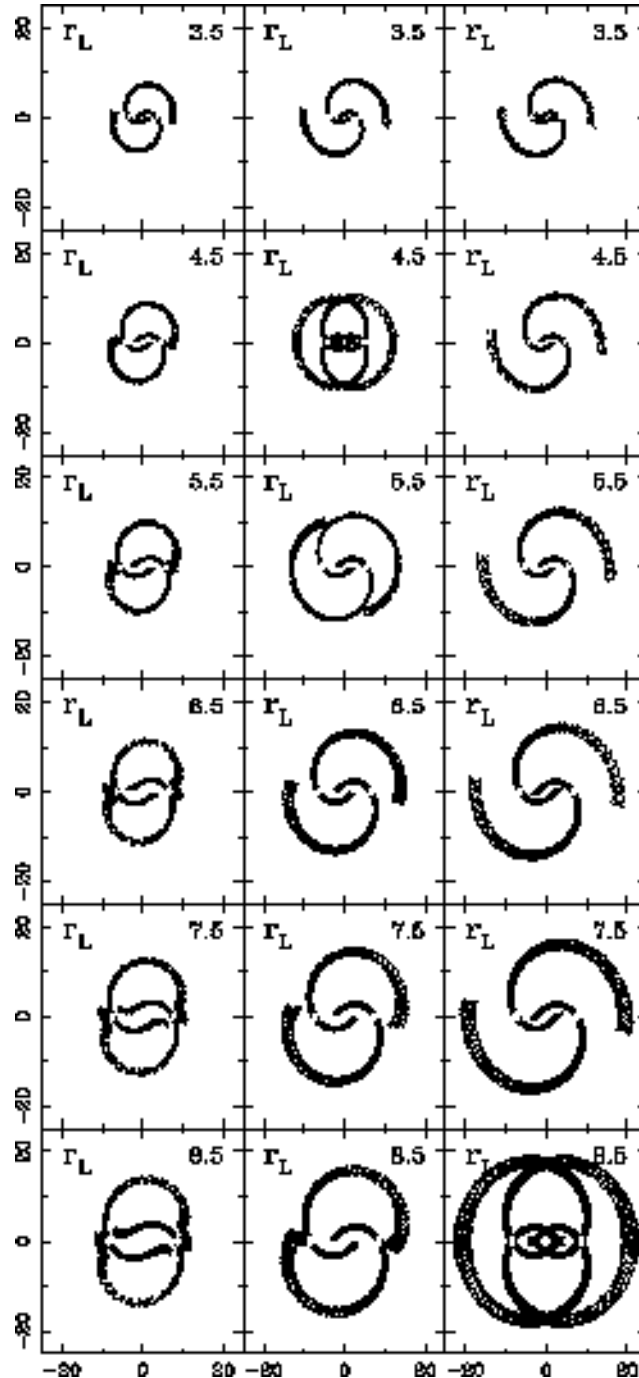


**Fig. 11.** Rings and spirals for three sequences of models with reference models R' (left), F' (middle) and D' (right), where we vary the Lagrangian radius,  $r_L$ . This value increases from top to bottom and is given in the upper right corner of each panel. The value of the strength parameter is fixed to  $\epsilon = 0.15$ . In all panels, we plot on the  $x - y$  plane the two unstable Lyapunov orbits associated to the unstable equilibrium points  $L_1$  and  $L_2$ , and the unstable invariant manifolds associated to the Lyapunov orbits, all for a given energy level. For model F' and  $r_L = 4.5$  and model D' and  $r_L = 8.5$ , we plot the corresponding stable invariant manifolds.

able, at this point, to foresee what morphology will result from each particular bar model and set of specific parameters without calculating the necessary invariant manifolds. The second unanswered point is to what extent the results found here are relevant to real galaxies. We have of course shown that the loci of the appropriate invariant manifolds can reproduce all the observed morphologies. This is very encouraging, but does not,

on its own, assure us that we have found here the theory that explains the formation of ring and spiral structures in barred galaxies. Several more points need to be considered before this conclusion can be reached. These yet unanswered two points will be addressed in Paper III.

**Acknowledgements** We thank Albert Bosma for stimulating discussions of the properties of observed rings. This work

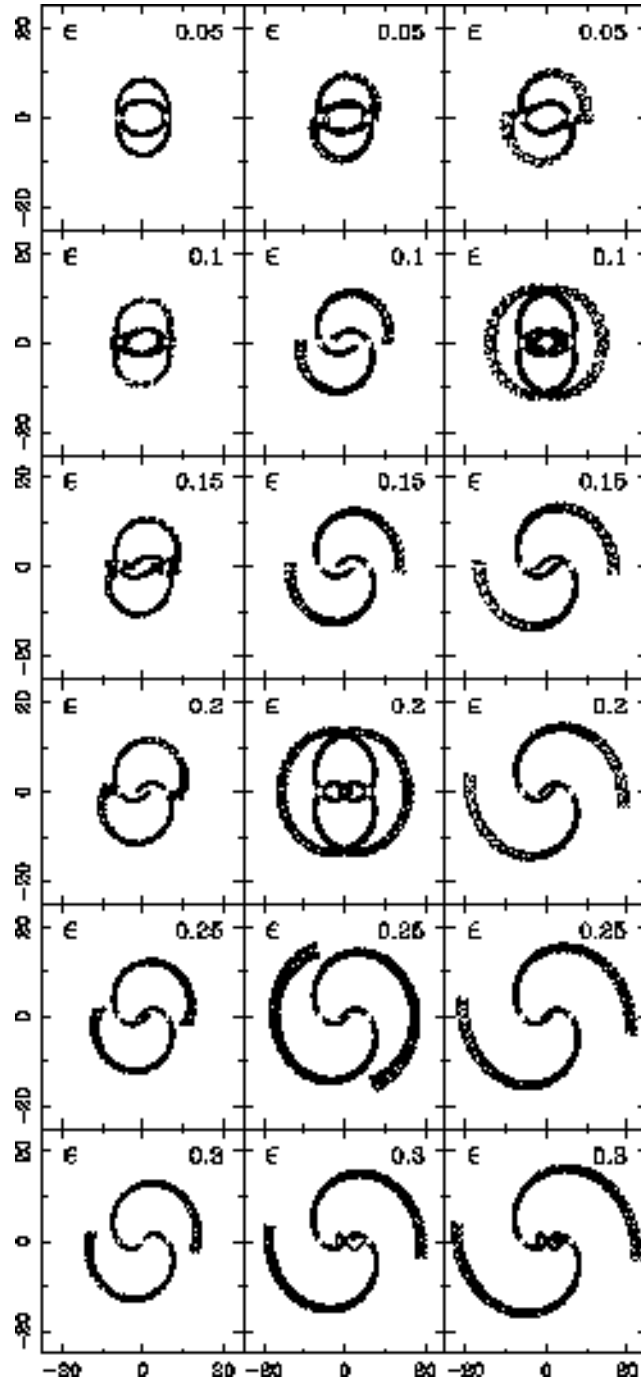


**Fig. 12.** Same as in Fig. 11 for three sequences of models with reference models R' (left), F' (middle) and D' (right) and different values of the bar strength parameter,  $\epsilon$ . The value of the Lagrangian radius is fixed to  $r_L = 6$ . For model F' and  $\epsilon = 0.2$  and model D' and  $\epsilon = 0.1$ , we plot the corresponding stable invariant manifolds.

is supported by the Spanish MCyT-FEDER Grant MTM2006-00478. MRG acknowledges her “Becario MAE-AECI”.

## References

- Athanassoula, E. 1980, *A&A*, 88, 184  
Athanassoula, E. 1984, *Phys. Rep.*, 114, 319  
Athanassoula, E. 1990 in “Galactic Models”, eds. J.R. Buchler, S.T. Gottesman and J.H. Hunter, *Annals of the New York Academy of Sciences*, Vol. 596, pp. 181-186  
Athanassoula, E. 1992a, *MNRAS*, 259, 328  
Athanassoula, E. 1992a, *MNRAS*, 259, 345  
Athanassoula, E., Bienaymé, O., Martinet, L., Pfenniger, D. 1983, *A&A*, 127, 349  
Barbanis, B., Woltjer, L. 1967, *ApJ*, 150, 461  
Binney, J., Tremaine, S. 1987, *Galactic Dynamics*, Princeton Univ. Press, Princeton  
Bosma, A. 1981, *AJ*, 86, 1791  
Buta, R. 1995, *ApJS*, 96, 39  
Buta, R., Crocker, D.A. 1991, *AJ*, 102, 1715  
Buta, R., Purcell, G.B. 1998, *AJ*, 115, 484

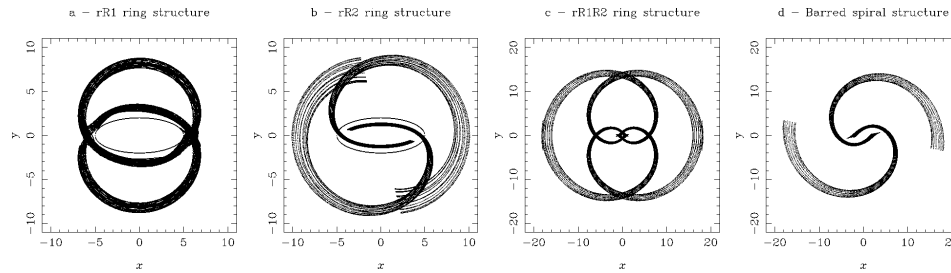


**Fig. 13.** Rings and spiral arms structures. We plot the invariant manifolds for different models. **(a)**  $rR_1$  ring structure with parameters: Model D with a Ferrers ellipsoid with  $n = 1$ ,  $a/b = 2.5$ ,  $r_L = 6$ ,  $Q_m = 4.5$ , and  $\rho_c = 0.05$ . **(b)**  $rR_2$  ring structure with model D, a Ferrers ellipsoid with  $n = 1$ ,  $a/b = 2.5$ ,  $r_L = 4.5$ ,  $Q_m = 4.5$ , and  $\rho_c = 0.05$ . **(c)**  $R_1R_2$  ring structure with model F' with a generalized Dehnen's bar potential,  $\epsilon = 0.24$ ,  $r_L = 6$ . **(d)** Barred spiral galaxy with model D' with a generalized Dehnen's bar potential,  $\epsilon = 0.15$ ,  $r_L = 6$ .

Buta, R., Byrd, G., Freeman, T., 2004, *AJ*, 127, 1982  
 Byrd, G., Freeman, T., Buta, R., 2006, *AJ*, 131, 1377  
 Contopoulos, G., Papayannopoulos, T. 1980, *A&A*, 92, 33  
 Contopoulos, G. 1981, *A&A*, 102, 265  
 Dehnen, W., 2000, *AJ*, 119, 800  
 Duval, M.F., Athanassoula, E. 1983, *A&A*, 121, 297  
 Elmegreen, D.M., Elmegreen, B.G., 1982, *MNRAS*, 201, 1021  
 Eskridge, P.B., Frogel, J.A., Podge, R.W., Quillen, A.C., Davies, R.L.,  
 DePoy, D.L., Houdashelt, M.L., Kuchinski, L.E., Ramírez, S.V.,  
 Sellgren, K., Terndrup, D.M., Tiede, G.P. 2000, *AJ*, 119, 536  
 Ferrers N. M. 1877, *Q.J. Pure Appl. Math.*, 14, 1  
 Fux, R., 2001, *A&A*, 373, 511  
 Gidea, M., Masdemont, J.J., 2007, to appear in *International Journal  
 of Bifurcation and Chaos*  
 Goldreich, P., Tremaine, S., 1978, *Icarus*, 34, 240  
 Goldreich, P., Tremaine, S., 1979, *ApJ*, 233, 857  
 Gómez G., Koon W.S., Lo M.W., Marsden J.E., Masdemont J.J., Ross  
 S.D. 2004, *Nonlinearity*, 17, 1571  
 Huntley, J.M., 1980, *ApJ*, 238, 524  
 Jörsäter, S., Moorsel, G.A. 1995, *AJ*, 110, 2037  
 Kaufmann, D.E., Contopoulos, G. 1996, *A&A*, 309, 381  
 Kormendy, J. 1982, in "Morphology and Dynamics of Galaxies", 12th  
 SAAS-FEE Course. Ed. by Martinet, L. and Mayor, M. Geneva  
 Observatory, p. 115-270.  
 Kranz, T., Slyz, A., Rix, H.W. 2003, *ApJ*, 586, 143  
 Kuzmin, G. 1956, *Astron. Zh.*, 33,27  
 Lindblad, B. 1963, *Stockholms Observatorium Ann.*, Vol. 22, No. 5  
 Lindblad, P.O. 1960, *Stockholms Observatorium Ann.*, Vol. 21, No. 4  
 Lindblad, P.A.B., Lindblad, P.O., Athanassoula, E. 1996, *A&A*, 313,  
 65  
 Lyapunov, A. 1949, *Ann. Math. Studies*, 17  
 Patsis, P.A., 2006, *MNRAS*, 369, L56  
 Patsis, P.A., Athanassoula, E., Quillen, A.C. 1997, *ApJ*, 483, 731  
 Pérez, I., Fux, R., Freeman, K. 2004, *A&A*, 424, 799  
 Pfenniger, D. 1984, *A&A*, 134, 373  
 Pfenniger, D. 1987, *A&A*, 180, 79  
 Pfenniger, D. 1990, *A&A*, 230, 55  
 Romero-Gómez, M., Masdemont, J.J., Athanassoula, E., García-  
 Gómez, C. 2006, *A&A*, 453, 39 (Paper I)  
 Sanders, R.H., Huntley, J.M. 1976, *ApJ*, 209, 53  
 Sanders, R.H., Tubbs, A.D. 1980, *ApJ*, 235, 803  
 Sandage, A., Bedke, J. 1994, *The Carnegie Atlas of Galaxies*,  
 Carnegie Inst. Washington  
 Schwarz, M.P. 1979, Ph.D. Thesis, Australian National University  
 Schwarz, M.P. 1981, *ApJ*, 247, 77  
 Schwarz, M.P. 1984, *MNRAS*, 209, 93  
 Schwarz, M.P. 1985, *MNRAS*, 212, 677

Skokos, Ch., Patsis, P.A., Athanassoula, E., 2002, *MNRAS*, 333, 847  
 Skokos, Ch., Patsis, P.A., Athanassoula, E., 2002, *MNRAS*, 333, 861  
 Toomre, A., 1963, *ApJS*, 138, 385  
 Toomre, A., 1969, *ApJ*, 158, 899  
 Toomre, A., 1977, *Ann. Rev. of A&A*, 15, 437  
 Toomre, A., 1981 in "The structure and evolution of normal galaxies",  
 eds. S.M. Fall and D. Lynden-Ball, Proc. of the Advanced Study  
 Institute, Cambridge, pp. 111-136  
 Toomre, A., Toomre, J. 1972, *ApJ*, 178, 623  
 Voglis, N., Stavropoulos, I., Kalapotharakos, C., 2006, *MNRAS*, 372,  
 901  
 Weiner, B.J., Sellwood, J.A., Williams, T.B. 2001, *ApJ*, 546, 931